

Acoustic attenuation, phase and group velocities in liquid-filled pipes: Theory, experiment, and examples of water and mercury

Kyungmin Baik,^{a)} Jian Jiang, and Timothy G. Leighton^{b)}

Institute of Sound and Vibration Research, University of Southampton, Highfield, Southampton, Hampshire SO17 1BJ, United Kingdom

(Received 8 July 2009; revised 26 August 2010; accepted 11 September 2010)

Del Grosso's [Acustica **24**, 299–311 (1971)] formulation, which predicts the phase speed of propagating axisymmetric modes inside a liquid-filled tube, is here extended to the complex domain in order to predict the attenuation, as well as the sound speed, of the modes as a function of frequency. Measurements of the sound speeds and the attenuations of the modes were performed in a water-filled Poly (methyl methacrylate) (PMMA) tube of internal radius, $b=4.445$ cm, in the range of the wavenumber-radius product, k_1b , from 2 to 10. Parts of three or four modes were investigated and the measured sound speeds and the damping of the modes were compared with the theoretical predictions. The theory was then used to estimate the modal sound speeds and attenuations in a stainless-steel pipe filled with mercury having the same dimensions as are used in the Spallation Neutron Source at Oak Ridge National Laboratory, Tennessee.

© 2010 Acoustical Society of America. [DOI: 10.1121/1.3495943]

PACS number(s): 43.30.Es, 43.20.Mv, 43.20.Hq, 43.30.Bp [DRD]

Pages: 2610–2624

I. INTRODUCTION

Experiment and theory are here used to predict the frequency-dependent attenuation and sound speed in mercury-filled steel pipelines surrounded by air, to support the development of acoustic sensors for the Spallation Neutron Source (SNS) at Oak Ridge National Laboratory (ORNL), Tennessee. To do this, Del Grosso's formulation¹ predicting the phase speed of the axisymmetric modes inside the liquid-filled tube, is extended to the complex space. Most earlier works quantified sound speed and not attenuation.^{2,3} Those which have calculated attenuation did so for mechanisms which are not significant in the ORNL scenario. These include radiation damping resulting from sound leakage into the surroundings (e.g., from water pipes into soil);^{4–6} losses due to the presence of a viscoelastic liner on the inside of a rigid pipe wall;⁷ viscous losses in an immersed coaxial multilayered cylinder;⁸ and viscous losses from the liquid in the pipe;⁹ Other analyses^{10–12} limit their consideration to thin-walled pipes or to the lower frequency range below the ring frequency (where the wavelength of the compressional wave in the wall equals the inner circumference of the tube).

The only study¹³ which resembled the ORNL scenario measured attenuation in a liquid-filled pipe surrounded by air, but did not present analysis for predicting it, instead comparing their measurements with the simulated output from a commercial software package. Given the peculiarities of mercury-filled steel pipes (where for example the mercury may resist wetting portions of the container or sensor immersed in it), the current manuscript develops such an analysis (which furthermore is of use since none of the above

studies mention typographical errors in the equations of the much-cited papers which form the basis of their studies).

Safety considerations preclude validating such a theory with mercury, and so validation was undertaken in water-filled poly (methyl methacrylate) (PMMA) pipe, which will be shown to exhibit sufficient similarities with the ORNL case. It should be emphasized that this consideration is restricted to compressional waves, and that other wave forms can occur in such structures.¹⁴

Although this paper is concerned with bubble-free liquids, the long-term goal for developing this approach was to measure bubble populations in pipelines from the extra attenuation caused by the presence of the bubbles compared to the attenuation in bubble-free pipelines. A key problem in estimating bubble populations acoustically is the often inappropriate use of free-field theory for data which is obtained in conditions which depart from the free field.¹⁵ While measurement of attenuation has proved effective for determining bubble populations in conditions which resemble free field,^{16–18} the requirement to compare the attenuation in bubbly conditions with that which would occur in bubble-free conditions, has meant that scattering (rather than attenuation) has more often been used to measure bubbles in conditions (like pipes) which depart from free field,^{15–22} since (as this paper illustrates) modeling for attenuation in liquid-filled pipes surrounded by air has not been common.

Section II describes the complex solution and shows its consistency with the works by Del Grosso¹ and Lafleur and Shields² in the inviscid limit. Section III describes the experimental method, and specifies the material properties and absorption used as input to the theory. Section IV shows that, in the frequency range studied here, measurements of the phase speeds of the modes agreed with the theoretical predictions, while the attenuations of the modes were measured overall to be greater than the theoretical predictions and had large uncertainties.

^{a)}Present address: Woods Hole Oceanographic Institution, Woods Hole, MA.

^{b)}Author to whom correspondence should be addressed. Electronic mail: tgl@soton.ac.uk

II. THEORY

A. Characteristic equation to axisymmetric modes

Lafleur and Shields calculated the dispersion relation of the axisymmetric propagation modes in a water-filled elastic tube with finite thickness based on the earlier work by Del Grosso.^{1,2} This approach has led to several useful innovations such as the development of a liquid-filled impedance tube.²³ Following earlier works which estimated the phase velocities of the axisymmetric modes in liquid-filled pipes having walls that were assumed to behave as thin shells,^{24,25} Del Grosso obtained the exact solution to the modes using the theory of elasticity.¹ He denoted those axisymmetric modes as ET*m* where ‘E’ and ‘T’ refer to the elastic wall and the finite thickness, respectively. Thus, the modes are identified by only one index *m* which indicates radial modes propagating along the tube axis. Equations (1a) and (1b) show the governing equations in an elastic tube and in a viscous liquid, respectively, in the absence of a body force.⁸

$$\rho_E \frac{\partial^2 \vec{S}_E}{\partial t^2} = (\lambda_E + \mu_E) \nabla (\nabla \cdot \vec{S}_E) + \mu_E \nabla^2 \vec{S}_E, \quad (1a)$$

$$\rho_L \frac{\partial^2 \vec{S}_L}{\partial t^2} = \left[\rho_L C_1^2 - i\omega \left(\frac{\eta}{3} + \eta_B \right) \right] \nabla (\nabla \cdot \vec{S}_L) - i\omega \eta \nabla^2 \vec{S}_L, \quad (1b)$$

where \vec{S} is displacement vector (the subscripts ‘L’ and ‘E’ denote that the terms relate to the liquid and the elastic tube, respectively), μ_E and λ_E are the Lamé constants of the tube material, ρ_E and ρ_L are the densities of the tube material and the liquid, respectively, and C_1 is the intrinsic speed of sound in the liquid. The coefficients η and η_B represent the shear and bulk viscosities of the liquid, respectively. In an elastic tube and a viscous liquid, a displacement vector \vec{S} can be expressed by the scalar potential, ϕ , and vector potential, $\vec{\psi}$, as $\vec{S} = \nabla \phi + \nabla \times \vec{\psi}$. In axisymmetric cylindrical coordinates, Elvira-Segura⁹ showed the resulting displacement vectors in the liquid and the elastic wall are as follows:

$$\vec{S}_L = - \left\{ \left[\frac{X_{0m}}{b} J_1 \left(\frac{rX_{0m}}{b} \right) \right] D_1 + [iq_{0m} J_1(\epsilon r)] D_2 \right\} \hat{r} + \left\{ [iq_{0m} J_0 \left(\frac{rX_{0m}}{b} \right)] D_1 + [\epsilon J_0(\epsilon r)] D_2 \right\} \hat{z}, \quad (2a)$$

$$\vec{S}_E = - \{ P_m [A_1 J_1(rP_m) + A_2 Y_1(rP_m)] + iq_{0m} [B_1 J_1(rT_m) + B_2 Y_1(rT_m)] \} \hat{r} + \{ iq_{0m} [A_1 J_0(rP_m) + A_2 Y_0(rP_m)] + T_m [B_1 J_0(rT_m) + B_2 Y_0(rT_m)] \} \hat{z}. \quad (2b)$$

While Elvira-Segura used a $+j\omega t$ convention, the $-i\omega t$ notation is adopted throughout this paper (the definitions of the variables therefore transpose between the two papers by use of the substitution of $i \leftrightarrow -j$). Note that a typographical error occurs in the viscous terms associated with the coefficient, D_2 in Elvira-Segura’s paper.⁹ A detailed description of that error can be found in Baik *et al.*²⁶ The radial displacement is composed of first order Bessel functions, J_1 and Y_1 , and the

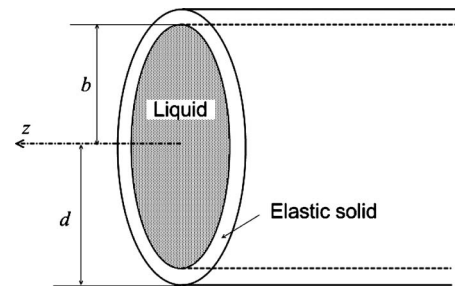


FIG. 1. Geometry of infinite liquid cylinder. Inner and outer radii are b and d , respectively.

axial displacement consists of zeroth order Bessel functions, J_0 and Y_0 . The factor, $\exp[i(q_{0m}z - \omega t)]$ (where q_{0m} is the complex axial wavenumber), is common to each term and it was omitted to simplify the notation. The ‘0’ in the subscript ‘0*m*’ refers to the mode being uniform along the circumference (i.e., an axisymmetric mode) and ‘*m*’ refers to the mode index. The variables are defined as

$$P_m^2 = k_c^2 - q_{0m}^2, \quad T_m^2 = k_s^2 - q_{0m}^2, \quad \epsilon^2 = \frac{i\rho_L \omega}{\eta} - q_{0m}^2, \quad \left(\frac{X_{0m}}{b} \right)^2 = k_1'^2 - q_{0m}^2, \quad k_1'^2 = \left[\frac{1}{k_1^2} - \frac{i}{\rho_L \omega} \left(\frac{4}{3} \eta + \eta_B \right) \right]^{-1}, \quad (3)$$

where $k_c = \omega/C_c$, $k_s = \omega/C_s$, and $k_1 = \omega/C_1$. The terms C_c and C_s represent the propagation velocities of longitudinal and shear waves, respectively, in the tube material (those are generally complex, see Sec. II C for detail). When the effects of liquid viscosity are minor, the complex wavenumber k_1' can be approximated as

$$k_1' \approx k_1 + i \frac{\omega^2}{2\rho_L C_1^3} \left(\frac{4}{3} \eta + \eta_B \right). \quad (4)$$

The imaginary part of the complex wavenumber is equivalent to the expression for the classical absorption in liquid.²⁷ Figure 1 shows the liquid-filled elastic tube with inner and outer radii b and d , respectively. In this geometry, the stress tensor elements are calculated as follows:

$$\tau_{rr} = \lambda \left(\frac{\partial S_r}{\partial r} + \frac{S_r}{r} + \frac{1}{r} \frac{\partial S_\theta}{\partial \theta} + \frac{\partial S_z}{\partial z} \right) + 2\mu \frac{\partial S_r}{\partial r}, \quad (5a)$$

$$\tau_{r\theta} = \mu \left(\frac{1}{r} \frac{\partial S_r}{\partial \theta} + \frac{\partial S_\theta}{\partial r} - \frac{S_\theta}{r} \right), \quad (5b)$$

$$\tau_{rz} = \mu \left(\frac{\partial S_r}{\partial z} + \frac{\partial S_z}{\partial r} \right). \quad (5c)$$

In a viscous liquid, λ and μ are equivalent to $\rho_L C_1^2 - i\omega(\eta_B - 2\eta/3)$ and $-i\omega\eta$, respectively.⁸ The six boundary conditions imposed in Eqs. (2) and (5) generate the six separate equations associated with the coefficients, A_1 , A_2 , B_1 , B_2 , D_1 , and D_2 . Boundary conditions describe the continuity of the displacement and the stress at both $r=b$ and $r=d$ in Fig. 1. Shear displacement is not considered in the lossless case. However, in the case of finite viscosity, a *no slip* condition is

included and this requires continuity of the shear displacement and stress at the liquid-tube interface.

The non-trivial solutions to the modes can be obtained by making the determinant of a 6×6 matrix equal to zero. The components of the 6×6 matrix are the terms associated with the individual constants $A_1, A_2, B_1, B_2, D_1,$ and D_2 . Therefore, expanding the determinant of a 6×6 matrix, the characteristic equation which describes the propagation of the wave inside the cylindrical tube filled with viscous liquid is given by following summation:

$$\begin{aligned}
 & d_{11}^p d_{21}^q d_{33}^r d_{43}^s L_{qp}(P_m) L_{sr}(T_m) + d_{13}^p d_{23}^q d_{31}^r d_{41}^s L_{qp}(T_m) L_{sr}(P_m) \\
 & - d_{11}^p d_{23}^q d_{33}^r d_{41}^s L_{sp}(P_m) L_{qr}(T_m) \\
 & - d_{13}^p d_{21}^q d_{31}^r d_{43}^s L_{sp}(T_m) L_{qr}(P_m) \\
 & - \frac{4}{\pi^2 P_m T_m b d} [d_{11}^{(0)} d_{31}^{(1)} - d_{11}^{(1)} d_{31}^{(0)}] [d_{23}^{(0)} d_{43}^{(1)} - d_{23}^{(1)} d_{43}^{(0)}] \\
 & - \frac{4}{\pi^2 P_m T_m b d} [d_{21}^{(0)} d_{41}^{(1)} - d_{21}^{(1)} d_{41}^{(0)}] [d_{13}^{(0)} d_{33}^{(1)} - d_{13}^{(1)} d_{33}^{(0)}] = 0,
 \end{aligned} \tag{6}$$

where $L_{mn}(y) = J_m(dy)Y_n(by) - J_n(by)Y_m(dy)$. The left side of the above equation is summed over the indices of $p, q, r, s = (0)$ and (1) . The superscripts (0) and (1) identify that the coefficient in question is associated with the zeroth (J_0 or Y_0) or first (J_1 or Y_1) order Bessel functions, respectively. Detailed expressions of each element of $d_{ij}^{(0),(1)}$ are given in Appendix A.

Figure 2 shows the numerical calculations of the group velocities and the attenuations of the axisymmetric modes in a copper pipe with 6.8 mm inner radius and 0.7 mm wall thickness filled with castor oil. The complex solutions to q_{0m} (solid curves) were found from Eq. (6). These are compared with the measurements by Aristégui *et al.*¹³ indicated as closed circles. The real and the imaginary parts of the complex solution give phase speed and the attenuation of the modes, respectively. These calculations assume no material absorption in the tube and the bulk viscosity, η_B , was ignored (see Sec. II C for details). The values used as input parameters are; $\rho_E = 8.933 \text{ g/cm}^3$, $C_c = 4.759 \text{ km/s}$, $C_s = 2.325 \text{ km/s}$ for copper¹³ and $\rho_L = 0.95 \text{ g/cm}^3$, $C_1 = 1.500 \text{ km/s}$, $\eta = 9.86 \text{ P}$ (this shear viscosity was estimated at 20°C by extrapolation using the data in the Reference 28 and it is about 1000 times larger than that of water) for castor oil.²⁸ Group velocities were found from the phase speed using Eq. (8) and are normalized with respect to C_1 . Numerical calculations obtained from Eq. (6) match well with the measurements in a viscous liquid cylinder by Aristégui *et al.* In Fig. 2(b), the ET0 attenuation has been added (it is not shown in the paper by Aristégui *et al.*) and it shows larger attenuation than the ET1 attenuation for frequencies less than about 130 kHz.

B. Lossless solutions to the characteristic equation

Lossless solutions to the modes can be found from Eq. (6) in the inviscid limit where η and η_B go to zero (which means $\epsilon \rightarrow \infty$). In this limit, $J_0(\epsilon b)$, $J_1(\epsilon b)$, and $J_1(\epsilon b)/[\epsilon b J_0(\epsilon b)]$ converge to zero, which makes each ele-

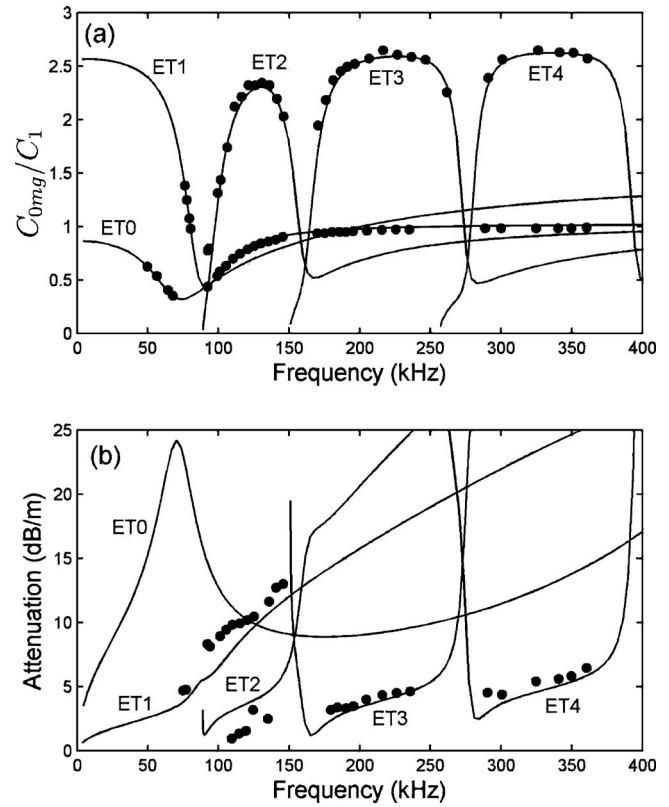


FIG. 2. (a) Normalized group velocities and (b) the attenuation of the axisymmetric modes in castor oil-filled copper pipe as a function of frequency. Those are obtained by Eq. (6). Material properties of copper and castor oil are described in Sec. II A. Group velocities were found from the calculated phase speeds using Eq. (8) and are normalized with respect to the intrinsic velocity in liquid. Measurements by Aristégui *et al.*¹³ are superposed as closed circles for comparison and they show good agreement with the theory.

ment of $d_{ij}^{(0),(1)}$ reduce to the form shown in Appendix B, and Eq. (6) simplify to a form consistent with the formulations given by Del Grosso¹ and Lafleur and Shields.² In these circumstances, at a given frequency, a series of real axial wavenumbers, q_{0m} , exist which satisfies Eq. (6) with the elements in Appendix B. The phase velocity, $C_{0m} = \omega/q_{0m}$, is calculated from the largest value of the q_{0m} , where the mode index, m , is $0, 1, 2, \dots$

Figure 3(a) shows the phase velocity of the axisymmetric modes in the water-filled PMMA pipe with $b = 4.445 \text{ cm}$ and $d - b = 0.5 \text{ cm}$ as a function of normalized frequency (wavenumber-radius product), $k_1 b$. The filled circles correspond to the lossless solution to Eq. (6) with the elements in Appendix B and the solid curves are the calculated phase velocities of the modes obtained from the real part of the complex solutions (see Sec. II C). The material properties assumed for PMMA are shown in Table I.^{29,30} The open circles and squares shown in the ET0 and ET1 calculations are obtained by choosing different sets of elastic constants of the PMMA other than the values in Table I (see Sec. III for details). Figure 3(b) shows the axisymmetric modes obtained from the complex solution in a water-filled aluminum pipe (a more rigid wall material than PMMA) with the same dimension as the PMMA pipe. A detailed description of the water/aluminum case is given in Sec. III. One mode denoted as the ET0 is subsonic. Other, higher, modes are all

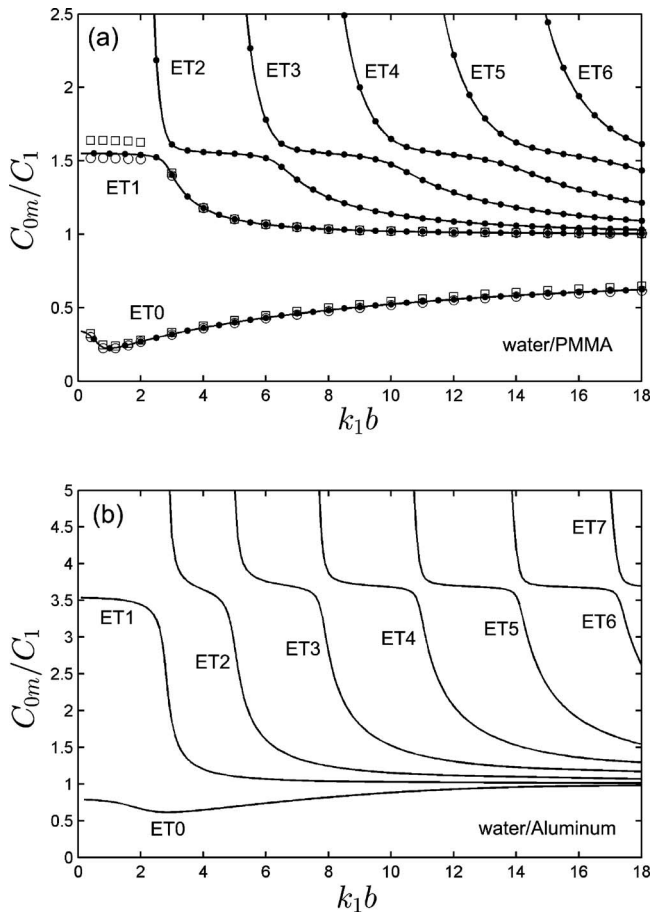


FIG. 3. Normalized phase velocities of the axisymmetric modes (a) in the water-filled PMMA pipe and (b) in the water-filled aluminum pipe as a function of normalized frequency. Dimensions of the tubes in both cases are the same. One subsonic mode named ET0 and one supersonic mode named ET1 exist down to zero frequency limit. Filled circles in (a) are lossless solution and solid lines are calculations obtained from the real part of the complex solution. The material properties of the PMMA^{29,30} and the aluminum⁴¹⁻⁴³ tubes are shown in Table I. The open circles and squares in the ET0 and ET1 calculations in (a) are obtained by using, in place of the PMMA values shown in Table I, different values which represent physically realistic variations in PMMA properties (see Sec. III for details).

supersonic. All modes tend eventually to the sound speed in the bulk liquid at the high frequency limit. In the ET0 mode, the acoustic interaction between the liquid and the wall happens in such way that coupling along the axial direction is always in phase, while those for other modes are out of phase over most of the frequency range. As a result, the ET0 mode acts as if the compressibility in liquid has increased, which makes it slower than the other modes.

As the frequency decreases, the phase velocities of ET2 and the higher modes become so large as to be undefined at their cut-off frequencies. These frequencies are evaluated by

TABLE I. Elastic properties of the elastic solids and water (Refs. 29 and 30).

Material	Density (g/cm ³)	C _c (km/s)	C _s (km/s)	C _b (km/s)	C _{pl} (km/s)	Poisson's ratio
PMMA	1.19	2.690	1.340	2.189	2.324	0.335
Aluminum	2.71	6.320	3.140	5.133	5.450	0.336
Water	1.00	1.479				

TABLE II. Cut-off frequencies of the modes in water/PMMA and mercury/steel pipes in dimensionless frequency k_1b .

Mode	ET2	ET3	ET4	ET5	ET6	ET7
Water/PMMA	2.234	4.938	7.792	10.730	13.722	16.744
Mercury/steel	2.530	5.330	8.249	11.215	14.213	17.235

taking the leading terms in Eq. (6) with the elements in Appendix B as q_{0m} goes to zero, which gives

$$bdk_s^4 L_{00}(k_c) - 2k_c k_s^2 [bL_{10}(k_c) + d(1 + Q_m^c b)L_{01}(k_c)] + 4k_c^2(1 + Q_m^c b)L_{11}(k_c) = 0, \quad (7)$$

where

$$Q_m^c = \frac{\rho_L k_s^2 J_0(k_1 b)}{2\rho_E k_1 J_1(k_1 b)}.$$

The cut-off frequencies of several modes calculated from Eq. (7) are listed in Table II in terms of the dimensionless frequency, k_1b . Figure 4(a) shows C_{0mg} , the group velocities of the modes inside the water-filled PMMA tube, converted from the phase velocities using the following equation:³¹

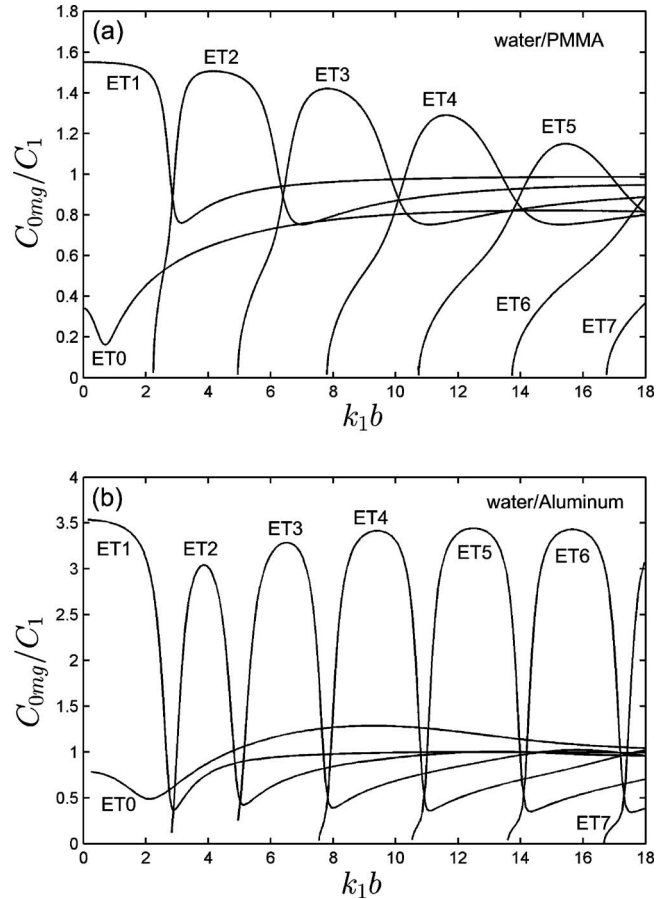


FIG. 4. Normalized group velocities of the axisymmetric modes (a) in the water-filled PMMA pipe and (b) in the water-filled aluminum pipe as a function of normalized frequency. These are converted³¹ from the calculated phase speeds shown in Fig. 2. At each cut-off frequency (ET2 and higher modes), the group velocity of the mode approaches zero while its phase velocity becomes infinite.

$$\frac{C_{0mg}}{C_1} = \frac{C_{0m}}{C_1} \left[1 - \frac{1}{1 - \frac{C_{0m}/C_1}{k_1 b \frac{d(C_{0m}/C_1)}{d(k_1 b)}}} \right]. \quad (8)$$

From Eq. (8), when the gradient of the phase speed $d(C_{0m}/C_1)/d(k_1 b)$ is almost zero, the group velocity becomes nearly the same as the phase velocity, which represents the plateau region of the phase speed of the mode. Moreover, following the characteristics of the modal phase velocities of Figs. 3 and 12(a), the group velocities of the modes attain maxima in the plateau regions, which can be deduced from Eq. (8) where the bracketed term tends to unity at high frequency. Comparing Fig. 3(a) with Fig. 12(a), the plateau regions of the modes are observed in a lower frequency range in the mercury/steel case than in the water/PMMA case. As the frequency approaches the cut-off frequencies of the ET2 and higher modes, the group velocities of the corresponding modes converge to zero while the phase velocities become infinite. However, the ET0 and ET1 modes do not have cut-off frequencies, but have finite solutions at the zero frequency limit. As $k_1 b \rightarrow 0$, Eq. (6) with the elements in Appendix B is reduced to

$$(3\beta - 4\alpha)yx^4 - \{4\gamma(\beta - \alpha) + [(3\beta - 4\alpha)(1 + \gamma) + \beta(\beta - \alpha)]y\}x^2 + \beta^2\gamma + \beta(\beta - \alpha)(1 + \gamma)y = 0, \quad (9a)$$

where

$$\alpha = \left(\frac{C_1}{C_c}\right)^2, \quad \beta = \left(\frac{C_1}{C_s}\right)^2, \quad \gamma = \frac{\rho_L}{\rho_E}, \quad x = \frac{C_1}{C_{0m}}, \quad y = \frac{d^2}{b^2} - 1. \quad (9b)$$

Equation (9) is identical to Eq. (6) of Lafleur and Shields² except where the latter contains a typographical error. A detailed description of this [and two other errors in their Eq. (4)] can be found in Baik *et al.*²⁶ Eq. (9) has quadratic form and thus it possesses two positive nonzero solutions to the ET0 and ET1 at the zero frequency limit as $C_{00}/C_1=0.343$ and $C_{01}/C_1=1.552$ for the PMMA/water tube used in the current paper, and these concur with the results shown in Fig. 3(a). Table I shows the bar wave speed, C_b , and the longitudinal thin plate velocity, C_{pl} , of PMMA. Normalizing those by C_1 reveals that $C_b/C_1 \approx 1.480$ and $C_{pl}/C_1 \approx 1.571$. Comparing these with the phase speed of the ET1 mode, at the zero frequency limit, C_{01}/C_1 is closer to the thin plate velocity than to the bar wave velocity, which means that the PMMA tube in this study acts more like a thin plate. Propagation of the mode (phase speed and attenuation) in this bubble-free pipeline is affected by the wall thickness. As frequency increases, the tube wall acts in a more rigid manner, such that all the phase speeds of the modes approach C_1 as the frequency becomes much greater than the cut-off for that mode and the thickness of the tube is no longer important to the mode propagation. However, as frequency decreases, when the thickness of the tube is small, mode propagation occurs in a thin plate-like manner, while propagation in a thick tube resembles solid bar-behavior. Consequently the phase speed and the attenuation of the modes are affected more by the tube thickness in the low frequency range.

C. Complex solutions to the characteristic equation

In practice, acoustic attenuation in a pipe can be extremely important (for example, where signals are passed down pipes for communication, leak detection in water pipes,³² in shock tubes,^{33,34} for the remote boundary characterization in waveguides,³⁵ and for the detection of the internal defects in pipes caused by chemical reactions, erosion, cracking, etc.¹⁴). In other circumstances, for example, the remote detection of buried tubes, the properties of both the pipe and the surrounding medium affect detection.^{36,37} Complex solutions for the axisymmetric modes in fluid-filled pipes were previously examined by several authors,¹⁰⁻¹² although their investigations were limited to the consideration of: (i) thin-walled shells, neglecting bending; (ii) the lower frequency range below the ring frequency (where the wavelength of the compressional wave in the wall equals the inner circumference of the tube); or (iii) the case when the outer surface of a pipe is surrounded by fluid in which all the losses are assumed to occur, such that the radiation damping can be found in the complex space but no damping is predicted when the surrounding fluid is vacuum or air.⁴ The current paper highlights the applicable implementation of the complex solutions to the fluid-filled pipe without such limitations on the wall thickness and frequency in the case that the outer surface of the tube is surrounded by vacuum or air. Although, as stated in the Introduction, the long-term goal is to invert the extra attenuation cause the bubbles in pipelines to estimate their population, this paper deals with the first stage of that process, and consequently this subsection outlines the theory by which this attenuation can be predicted in bubble-free pipelines. The complex solutions to the modes inside the liquid tube are obtained by expanding real wavenumbers, k_s and k_c , in Eq. (6) to complex wavenumbers, k'_s and k'_c as follows:

$$k'_s = \frac{\omega}{C_s}(1 + i\gamma_s), \quad k'_c = \frac{\omega}{C_c}(1 + i\gamma_c), \quad (10)$$

where γ_s and γ_c are the normalized shear and longitudinal absorption coefficients, respectively. Those of the PMMA are $\gamma_c=0.0034$ and $\gamma_s=0.0053$ derived from the measurements by Hartmann and Jarzynski.^{29,30} When the tube is surrounded by liquid, damping occurs as a result of the radiation into the surrounding liquid. In that case, regardless of the presence of the liquid inside the tube, radiation damping can be found without introducing the absorption⁴ in the elastic solids as was done in Eq. (10). However, when the surrounding liquid is substituted by air or vacuum as in this study, the wavenumbers in the elastic solid should be extended to the complex space to obtain the attenuation of the modes. The absorption in bulk water is embedded in k'_l of Eq. (3) because in pure water at the frequencies used in the experiment, viscous damping provides the dominant mechanism for acoustic absorption. Therefore, substituting those complex wavenumbers into Eq. (6), at a given frequency, $q'_{0m} = \omega/C_{0m} + i \text{Im}[q'_{0m}]$ is found in the complex domain. The real part of q'_{0m} gives the phase velocities of the modes, and the normalized phase velocity of the mode can be calculated using $C_{0m}/C_1 = k_1/\text{Re}[q'_{0m}]$. The imaginary part of q'_{0m} gives the

damping of the corresponding modes, and the attenuation coefficients, in units of dB per unit length, is calculated by $20 \text{Im}[q'_{0m}] \log(e)$.

The implementation of Eq. (6) can sometimes be problematical in numerical precision since the viscosity coefficients, η and η_B , are usually very small in the case studied here. As a result, the corresponding value of ϵ generates a complex quantity of which the imaginary part is much larger than the real component. The order of the magnitude of the normalized quantity, ϵ/k_1 , is about 10^3 – 10^4 even in the range of a few hundred kHz in the case of water. In such circumstances the inviscid limit in Eq. (6) can be adopted. Furthermore, the complex wavenumber in the bulk liquid, k'_1 , can be approximated as Eq. (4). Therefore, when the acoustic excitation makes such circumstances hold, the elements in Appendix B can be used instead of the elements in Appendix A in Eq. (6) to obtain the complex solution by substituting k_s, k_c , and k_1 with k'_s, k'_c , and k'_1 into the elements in Appendix B.

The solid curves in Fig. 3(a) show the phase velocities of the modes calculated from the real parts of the complex solutions. Lossless solutions are denoted as filled circles which on this scale are indistinguishable from the solid lines—the typical discrepancy is the order of $10^{-6}\%$. Because the loss is only accounted for by the imaginary part of the wavenumber, which is much smaller than the real part of the wavenumber, the introduction of the complex wavenumbers (k'_s, k'_c, k'_1 , and q'_{0m}) into the formulation does not alter the predicted phase speeds of the modes significantly compared to the lossless solution. This can be examined by considering the Taylor expansion of the characteristic equation. Denote the left side of Eq. (6) as $\Xi(k_m, q_{0m})$ where k_m represents the wave numbers of the input parameters such as k_c, k'_c , etc. that can be complex. Then Eq. (6) is expressed as $\Xi(k_m, q_{0m}) = 0$ and the solution is given by the value of q_{0m} which satisfies this condition. Hence, for a real parameter, k_p , the lossless solution q_{0p} satisfies $\Xi(k_m=k_p, q_{0m}=q_{0p})=0$. Now suppose that the real wavenumber, k_p , is slightly varied as $k'_p = k_p + i\delta_p$ where δ_p is imaginary part of the complex wavenumber, k'_p , and $|\delta_p| \ll |k_p|$. Then, for a given input parameter of k'_p , the complex solution q'_{0p} can be found from the characteristic equation of $\Xi(k_m=k'_p, q_{0m}=q'_{0p})=0$. Suppose furthermore that $q'_{0p} = q_{0p} + i\Delta_p$ and $|\Delta_p| \ll |q_{0p}|$. Applying the Taylor expansion for this equation up to the second order of $\partial^2 \Xi$, the relation becomes

$$\begin{aligned} \Xi(k'_p, q'_{0p}) \approx & \Xi(k_p, q_{0p}) + (i\delta_p) \left. \frac{\partial \Xi}{\partial k_m} \right|_{k_m=k_p, q_{0m}=q_{0p}} \\ & + (i\Delta_p) \left. \frac{\partial \Xi}{\partial q_{0m}} \right|_{k_m=k_p, q_{0m}=q_{0p}} + \frac{1}{2} \left[(i\delta_p)^2 \frac{\partial^2 \Xi}{\partial k_m^2} \right. \\ & + (i\Delta_p)^2 \frac{\partial^2 \Xi}{\partial q_{0m}^2} \\ & \left. + 2(i\delta_p)(i\Delta_p) \frac{\partial^2 \Xi}{\partial k_m \partial q_{0m}} \right]_{k_m=k_p, q_{0m}=q_{0p}}. \end{aligned} \quad (11)$$

Hence, the real part and the imaginary part of the equation

should satisfy

$$(\delta_p) \left. \frac{\partial \Xi}{\partial k_m} \right|_{k_m=k_p, q_{0m}=q_{0p}} + (\Delta_p) \left. \frac{\partial \Xi}{\partial q_{0m}} \right|_{k_m=k_p, q_{0m}=q_{0p}} = 0, \quad (12a)$$

$$\begin{aligned} \Xi(k_p, q_{0p}) - \frac{1}{2} \left[(\delta_p)^2 \frac{\partial^2 \Xi}{\partial k_m^2} + (\Delta_p)^2 \frac{\partial^2 \Xi}{\partial q_{0m}^2} \right. \\ \left. + 2(\delta_p)(\Delta_p) \frac{\partial^2 \Xi}{\partial k_m \partial q_{0m}} \right]_{k_m=k_p, q_{0m}=q_{0p}} = 0. \end{aligned} \quad (12b)$$

Disregard of the second order ($\partial^2 \Xi$) in Eq. (12b) gives the condition $\Xi(k_p, q_{0p})=0$, which is identical to the lossless solution. However, when the second order terms are not negligible, the real part of the solution is no longer the same as the lossless solution. In such a case, any imaginary part of the input complex wavenumber, δ_p , is not negligible. This can for example be caused by significant absorption in the tube material in Eq. (10) or a sizable damping term in viscous liquid in Eq. (3). When this is the case, Eqs. (12a) and (12b) require amendments to the phase speed of the mode, which consequently is not the same as that given by the lossless solution.³⁸

For each complex solution of the mode, the corresponding imaginary part normalized by the wavenumber k_1 is shown in Fig. 5(a). As in Fig. 3(a), the open circles and squares in the ET0 and the ET1 calculations on Fig. 5(a) were obtained by choosing two different sets of values for the elastic constants of the PMMA other than those given in Table I (see Sec. III for details). Each mode exhibits a dip in attenuation across a limited frequency range. For example, this trend is observed in $2.3 < k_1 b < 2.9$ for ET2 mode, $4.9 < k_1 b < 6.5$ for ET3 mode, $7.8 < k_1 b < 10.3$ for ET4 mode, and so on.

The damping of the ET0 mode is larger than that of any other mode over most of the frequency range. The magnitude of the ET0 attenuation is at least three times that of the ET1 mode. It has the maximum attenuation around $k_1 b \approx 0.7$. Figure 5(b) shows the corresponding calculations for the water-filled aluminum tube discussed in Sec. III.

III. EXPERIMENTS AND MEASUREMENTS

Experiments are carried out in a water-filled PMMA tube of 2 m length, 4.445 cm inner radius, and 0.5 cm wall thickness. The shear and bulk viscosities of water were taken to be 0.89 cP and 3.09 cP, respectively.³⁹ The published properties of PMMA and water are shown in Table I.^{29,30} These are the values that were used in the calculations reported in this study, although the properties of the real materials may depart from these published values.⁴⁰ A sensitivity study was conducted [see the open circles and squares in Figs. 3(a) and 5(a)]. It showed that a variation of material properties within the published range for anisotropic PMMA⁴⁰ did not alter the trends outlined in this study over the parameter range studied here (though this may not hold at higher frequencies). The open circles are calculated from the lower published values of the longitudinal and shear speeds (2.604 km/s and 1.318

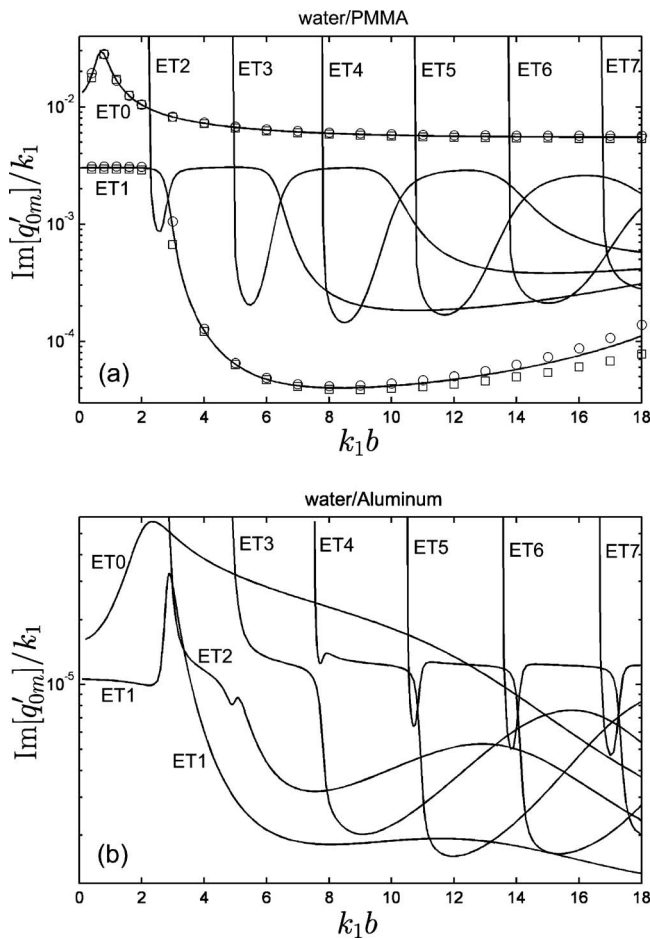


FIG. 5. Normalized damping of the axisymmetric mode (a) in the water-filled PMMA pipe and (b) in the water-filled aluminum pipe as a function of normalized frequency. This was obtained from the imaginary part of the complex solution to Eq. (6) with the elements in Appendix B. The open circles and squares in the ET0 and the ET1 calculations in (a) are obtained by allowing the material properties of PMMA used in the calculation to depart from those listed in Table I by physically realistic amounts (see Sec. III for details). The damping of the ET0 mode is larger than those of the any other modes.

km/s, respectively), and the open squares correspond to the higher published values (3.033 km/s and 1.388 km/s, respectively). As shown in Figs. 3(a) and 5(a), when allowing for the variance of the elastic constants, changes of the sound speeds and the attenuation in the ET0 and ET1 modes are negligible over most of the frequency range examined here. For the ET1 mode, the phase velocities at the higher frequency range of $k_1 b \geq 3$ for the three cases are nearly the same. This trend is also investigated in the corresponding damping factor of the ET1 mode [Fig. 5(a)]. The higher phase velocity results in the lower damping of the ET1 mode at the low frequency range but the variance is less than 5%. In a similar vein as the phase velocity results, the attenuations of the ET1 mode at the higher frequency range of $k_1 b \geq 4$ for the three cases are nearly the same. However, at large $k_1 b$, the attenuations of the ET1 mode diverge. For the ET0 mode, the variances of the phase velocities and the attenuations diverge at large $k_1 b$. The higher phase velocity results in the lower damping of the ET0 mode over the frequency range, and the attenuations in the frequency range of $1 \leq k_1 b \leq 3$ for the three cases are very similar [Fig. 5(a)].

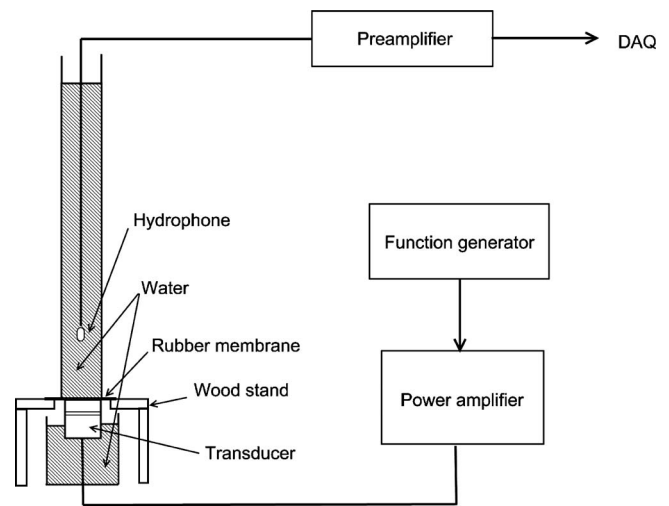


FIG. 6. Block diagram of the experimental setup for the measurement of the wave propagation in the liquid cylinder. Figure was not drawn in scale.

Numerical calculations were done for the case when aluminum is used in place of PMMA for a tube of exactly the same dimensions. This was done to show the effect of the tube material (Table I) on the phase and group speeds and the attenuation of the modes as shown in Figs. 3(b), 4(b), and 5(b). Ultrasonic absorption in metal is complicated and can vary with the type of the metal alloy, grain size, and temperature etc.^{41–43} In the calculations of Figs. 3(b), 4(b), and 5(b), normalized shear and longitudinal absorptions, γ_s and γ_c are found from one of the measurement by Mason,⁴¹ specifically $\gamma_s = 2.57 \times 10^{-5}$ and $\gamma_c = 8.50 \times 10^{-5}$. The liquid inside the aluminum tube is water. Since, as frequency increases, the tube wall acts in a more rigid manner, all the modes converge to C_1 at the high frequency limit. In the case of the aluminum/water tube [Fig. 3(b)], this convergence tends to occur at lower frequencies than it did for the PMMA/water tube [Fig. 3(a)] because aluminum is more rigid than PMMA. Figure 4(b) shows the group velocities of the modes converted from their phase velocities. One interesting feature investigated in the ET0 mode is that, although its phase speed is subsonic throughout the frequency range studied here, its group velocity is supersonic at some frequencies. The attenuations in the water/aluminum system [Fig. 5(b)] are about two orders of magnitude less than those in the water/PMMA case [Fig. 5(a)] since the ultrasonic absorption in aluminum is smaller than it is in PMMA.

Figure 6 shows the block diagram of the experimental setup. The tube is supported vertically. The height of the water column is $1.8 \text{ m} \pm 0.2 \text{ cm}$. An input signal is generated by the function generator (SRS DS345) which emitted tone bursts of varying frequencies, and was amplified by a power amplifier (ENI 2100L) to a source (Neptune Sonar 4008, SN 18852), which transmitted a pulse into the base of the water column via a neoprene membrane (1.5 mm thick CNE60). A hydrophone (Brüel & Kjaer 8103) is moved vertically along the axis inside the tube. Its signal is conditioned by a charge amplifier (Brüel & Kjaer 2635). At a given location of the hydrophone, the driving frequency of the function generator (here termed the ‘nominal’ frequency) was set to increment from 15 to 35 kHz in 1 kHz steps. The number

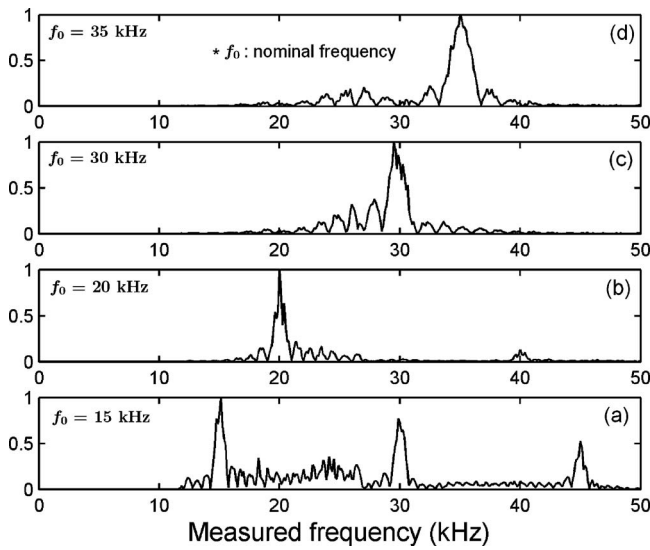


FIG. 7. Spectra of the hydrophone signal measured in the water-filled tube when the coupling to the pipe is involved for acoustic excitations set to nominal values of 15, 20, 30, and 35 kHz. The amplitudes of the spectra are drawn in linear scale (Volts/Hz) and are normalized by the maximum value of the spectrum within the frequency range on the picture at each nominal frequency. The spectral peak at each case is close to the nominal frequency of the acoustic excitation. Since the acoustic source has a resonance frequency at 25 kHz and its bandwidth is narrow, most of the secondary peaks are located between 20 and 30 kHz.

of cycles of the pulse was set to twenty to give the signal narrowband character (noting that the spectrum emitted by the function generator is shaped to produce the spectrum of the energy in the water by the transfer functions of the power amplifier and source, the latter being different from its free-field value because it is coupled to the tube). The example spectra are shown in Fig. 7. The amplitudes of the spectra are normalized by the maximum value of the spectrum within the frequency range on the picture. Spectral peaks are located at 14.95, 19.7, 29.5, and 35.04 kHz, respectively, though they were produced from signal generator outputs centered around 15, 20, 30, and 35 kHz, respectively (deviations from a flat amplitude and linear phase response in the hydrophone would cause negligible spectral changes over this frequency range). Note that even though the maximum drive setting was 35 kHz in the experiment, the loci of the modes in the $k-\omega$ map [Fig. 8(b)] exist to 54.5 kHz ($k_1 b = 10.3$) and so phase speed calculations are undertaken up to this limit (SNR is too low to use these data for attenuation).

Two options were investigated to obtain the sound speed. The first is the two dimensional Fourier transform (denoted as the $k-\omega$ method in this paper)⁴⁴ which is suitable for situations where the hydrophone moves along the length of the tube. The second is the PS (Phase Spectrum) method,^{45,46} which compares the signals from hydrophones at two or more fixed positions in the tube.

The $k-\omega$ method determines the phase speed of the mode from the 2D spectrum of the plot of wavenumber, k , against frequency, ω . This plot is obtained from the sequence of time histories recorded as the on-axis hydrophone is moved vertically in 1 cm increments from 20 cm above the bottom of the tube up to 30 cm below the air-water interface so that the total length of the hydrophone movement is 130

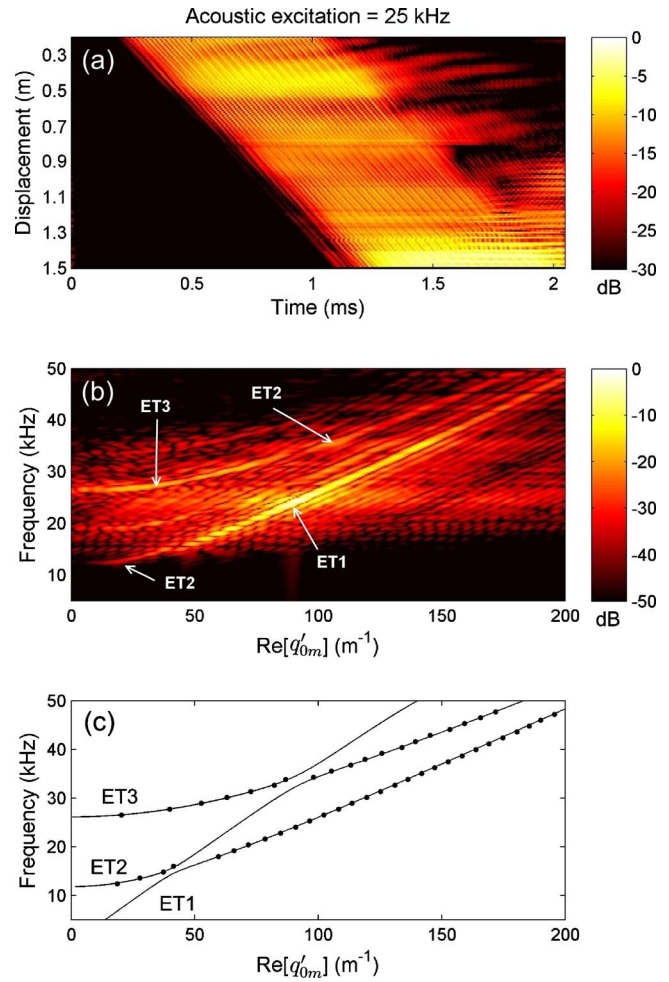


FIG. 8. (Color online) An example of the $k-\omega$ method. (a) Time series at 25 kHz of acoustic excitation, (b) 2D spectrum of the measurements, and (c) extracted dominant features (black dots) and the theoretical loci of the modes (solid curves).

cm (the 1 cm increments being appropriate for sampling up to 75 kHz according to the Nyquist sampling theorem applied to an infinite body of liquid). These time histories are stacked to form an array of time vs. hydrophone location at a given acoustic excitation frequency, with acoustic pressure amplitude shown with the color scale. This is shown in Fig. 8(a) (for the example of 25 kHz nominal excitation), and Fig. 8(b) shows the $k-\omega$ plot in dB scale that is formed by the sum of the magnitudes of the generated 2D spectra for all the acoustic excitation frequencies studied (from 15 kHz to 35 kHz). Several highlighted features are shown which correspond to the propagating axisymmetric modes in the tube. Local maximum values along those bright contours in Fig. 8(b) were sampled to determine the real part of the wavenumber q'_{0m} of the dominant modes as shown in Fig. 8(c). The black dots in Fig. 8(c) indicate the location of the local maximum values in $k-\omega$ space and those appear to be located close to the theoretical loci (solid curves) of the modes in $k-\omega$ space. The value of every vertical coordinate on the highlighted trace is the frequency, f in Hz, and the value of the every horizontal coordinate is the wavenumber, k in m^{-1} [in the notation of Eq. (7), this is equivalent to the real part of q'_{0m}]. The ratio of the one to the other (multiplied by 2π)

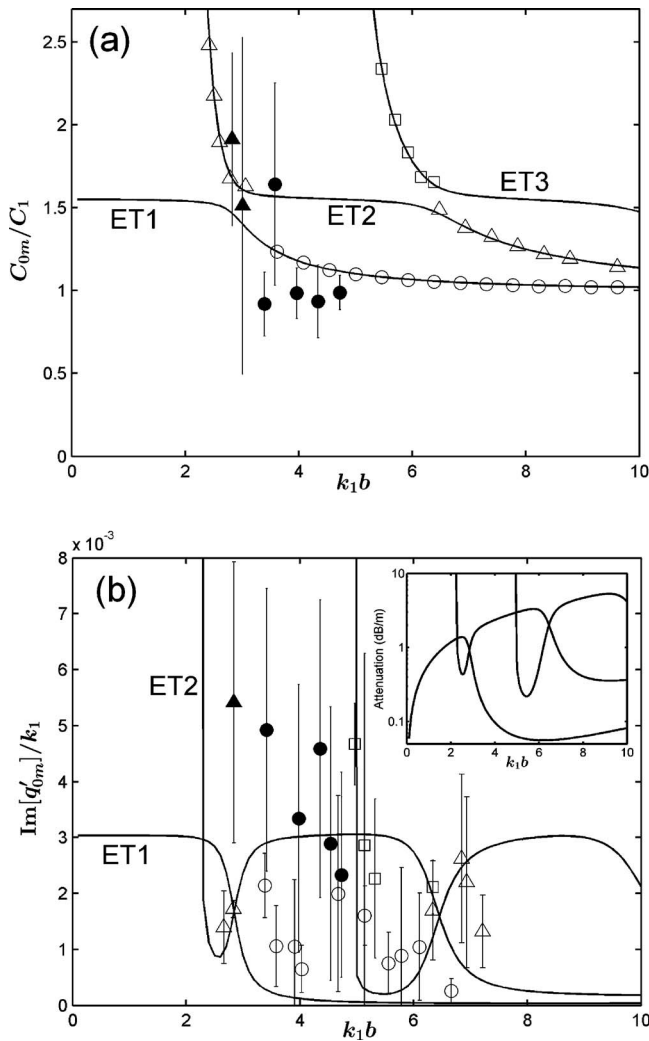


FIG. 9. Measured normalized (a) phase velocities and (b) damping of the modes (open symbols) calculated using the $k-\omega$ method from Fig. 8(c) and Prony's method. Theoretical modal dispersion curves are denoted as solid curves. Measurements of the phase velocities and damping by the PS method are denoted as filled symbols. Modes are assigned the following symbol shapes: ET1=circles, ET2=triangles; ET3=squares. The error bars for the open symbols in (a) were too small to be plotted (the maximum and the minimum deviations being about 5% and 0.04%, respectively). Detailed descriptions of the error bars are given in Sec. III.

gives $2\pi f/k$, the phase velocity of the mode at that frequency [Fig. 9(a)]. The instantaneous slope at that position (multiplied by 2π) gives the group velocity.

Once a mode is identified in the $k-\omega$ plot, this mode is extracted for the calculation of the attenuation. By allowing a specific mode to survive and eliminating other modes in the $k-\omega$ plot, the inverse Fourier transform of this modified $k-\omega$ spectrum along the wavenumber, k , generates the spectrum in the frequency vs. displacement of the hydrophone. This spectrum consists of only one specific mode. Then, Prony's method is applied to the complex signal along the displacement at each frequency slice⁴⁷⁻⁴⁹ to calculate the imaginary part of the complex wavenumber q'_{0m} [Fig. 9(b)].

Although moving the hydrophone along a tube is mechanically complicated, it has significant advantages over the more practically deployable technique of inserting hydrophones through the pipe walls (or fixing them inside the pipe) and taking measurements at the fixed positions (the PS

method). In using fixed sensors at specific points along the pipe, the PS method would seem to offer advantages to industrial deployment, or situations where hazardous material (e.g. mercury in the Spallation Neutron Source) necessitates minimum interference with the sensors once they are in place.⁵⁰ The PS method does not require a full scan of the hydrophone along the liquid column to obtain the phase velocity and the attenuation of the propagating wave. Instead, it investigates the phase differences between spectral components at a given acoustic excitation (f) measured at two separated locations (say z_1 and z_2).^{45,46} This phase difference is related to the wavenumber (k) of the mode, and the phase velocity (c_{phase}), is calculated by $c_{\text{phase}}=2\pi f/k$. Attenuation can be simply calculated by comparing the amplitudes of the spectra at z_1 and z_2 . The PS does not need as many measurements as the $k-\omega$ method, and yet despite all these practical advantages, it proved to be inferior to the $k-\omega$ method for undertaking the measurements described in this paper as shown in Figs. 9(a) and 9(b), which plot the predicted and measured phase velocities and attenuation, respectively. The measurements were done by the $k-\omega$ method (open symbols) and the PS method (filled circles). Note that one problem with implementing the PS method was that it was not accurate in the frequency range where two or more modes are mixed together, as this mixing generated ambiguities and errors. Furthermore, the outcome of the PS method is very sensitive to the choice of the two separated locations of the measurements (z_1 and z_2) unless the modes are completely decoupled. The error bars shown in the PS results denote \pm one standard deviation, the variation resulting from the sensitivity to the choice of the various values of z_1 and z_2 used in the calculation at a given frequency. Therefore for these tests the PS method was applied only in the frequency range of $2.8 < k_1b < 5$ where, for the most part, only one mode is investigated (the ET1 or ET2 mode). In Figs. 9(a) and 9(b), the $k-\omega$ method was repeated by truncating the sequence of the signals after a certain displacement [for example, truncating out the signals after 0.3 m and only taking the signal arrays between 0.2 m and 0.3 m in Fig. 8(a)]. At each step of this, the measured phase speed and attenuation of the modes by the $k-\omega$ method and Prony's method were different. Thus, at a given frequency, a distribution of the phase speed and attenuation by the length of the sequence of the signal was obtained. The average and the deviation of the modes were displayed as open symbols and error bars in Figs. 9(a) and 9(b) [in Fig. 9(a), error bars for the phase speeds of the modes obtained by the $k-\omega$ method were too small to be plotted, the maximum deviation being about 5%]. While the $k-\omega$ method (open symbols) gives good agreement with the predicted phase velocities (less than 5% discrepancy), the PS method (filled symbols) does not agree with the theory as well (even allowing for the larger error bars, which indicate the greater precision as well as accuracy, of the $k-\omega$ method). This trend is also observed in Fig. 9(b) [while the agreement between experiment and theory for the $k-\omega$ method (open symbols) is shown, the error bars and measurement by the PS method (solid symbols) show large errors and uncertainties associated with the modes]. The attenuations calculated by the PS method in the range of 4

$<k_1b < 5$ are at least eight times larger than the predicted theory (ET1). Below this frequency range, the PS method gives attenuations 2–3 times larger than those the predicted theory (ET2).

IV. DISCUSSION

If one did not have the assistance of the mode labels on the graph, the experimental data in Fig. 8(b) at first sight would appear to indicate two major curves [plus numerous subsidiary ones that are attributed to non-axisymmetric modes which are removed for clarity in Fig. 8(c)], but it would be incorrect to seek two modes against which to identify these curves. This is made clear in Fig. 8(c), where the agreement between the phase velocity predicted by theory (solid line) and experimental data of Fig. 8(c) [shown as open and filled symbols on Fig. 9(a)] allow identification of the mode associated with each data point. Recall that the algorithm by which these experimental data are processed does not identify the mode associated with each data point; rather such identification is made by the authors when comparing the position of each data point with theory, such that the assignment of symbol shape (corresponding to mode number) in Figs. 9(a) and 9(b) is manual. Consider the two curves of open symbol ($k-\omega$) data in Fig. 9(a). Each of these two loci of experimental data [which come from the two loci in Fig. 8(c)] is actually seen to cross two of the modes predicted by the theory, with subtle ‘break points’ where the data crosses from one mode to the next. Similar ‘break points’ are also observed in the dispersion curves inside the rectangular duct, calculated and simulated based upon the homogeneous thin plate theory restricted to the low frequency regime.^{51,52} Use of Fig. 9(a) in this way, therefore allows identification of the data in Fig. 8(c) with specific modes, and Fig. 8(c) is labeled using that identification. The subsonic ET0 mode is not detected. The ET1 mode is only observed at frequencies greater than 15 kHz, the locus of data points transitioning at this frequency [with a ‘break point’ which is clearly discernible in Fig. 8(b)] to the ET2 mode which extends down from 15 kHz to 12 kHz, which is close to the cut-off frequency of the ET2 mode as shown in Table II. Between 15 kHz to 30 kHz, the ET2 mode is not observed above the background noise, although it does reappear at frequencies greater than 30 kHz as a continuation [again via a ‘break point’ which is clearly visible in Fig. 8(b)] of the locus points formed by the ET3 mode between 26 kHz (close to cut-off frequency of the ET3 mode as shown in Table II) and 34 kHz. Above this frequency, it is hard to recognize the ET3 mode in the spectrum. Besides these three modes, no other axisymmetric modes are observed in the data.

The three possible reasons why certain modes are not observable in different frequency ranges (and the ET0 mode is not observed at all) are discussed below, in increasing order of importance.

The first reason is because the different frequency dependencies of attenuation of the various modes will mean that the signal-to-noise ratio of that mode, in a given frequency range, will be lower than outside of that range. As

shown in Fig. 5(a), the frequency ranges in which specific modes are not observable corresponds to the regions of higher attenuation. However the absolute changes in attenuation are probably not sufficiently great to eliminate observation of these modes over the measurement distances used in the experiment. Hence other contributory factors must be considered, as discussed below.

The second reason is owing to the limited energy input as shown in Fig. 7. The free field calibration⁵³ curve of the acoustic source indicates the resonant frequency as 24.5 kHz and FWHM (Full Width at Half Maximum) as narrow as 3 kHz. Figures 7(a)–7(d) show sample spectra in the water when this source is coupled to the pipe for nominal frequencies of 15, 20, 30, and 35 kHz respectively. The spectra show energy at frequencies other than that of the nominal excitation (the source being efficient in the 20 kHz–30 kHz range). The sensitivity at the higher frequency range such as $k_1b = 8.5$ (45 kHz where damping of the ET4 is expected to be minimum) is poor in our system because the frequency of the acoustic excitation used is from 15 kHz to 35 kHz.

The third reason is probably the most potent. Over the frequency range of interest, each axisymmetric mode has a particular shape configured by the longitudinal and the axial motions of the infinitesimal elements in the liquid and the elastic solid. When the acoustic source cannot support those motions, it cannot strongly excite the mode having such motion. The acoustic source used here is piston-like and its diameter is about 3 in. which is less than the inner diameter of the tube (3.5 in.). Although the rubber membrane (Fig. 6) is in contact both with the liquid and the PMMA, the source will not excite the PMMA efficiently. Figure 10 shows the calculated amplitudes of the axial (longitudinal) displacements of the ET0 and ET1 modes both in water and the PMMA as a function of the distance from the center of the tube normalized by the inner radius of the tube [see Eqs. (8) and (10) in Ref. 2 for the explicit expression of the axial displacements]. The amplitudes were normalized by the amplitude of the axial displacement at the center ($r=0$). The axial component of the displacement vectors in water and PMMA were calculated for the lossless case. Hence, the axial displacements are discontinuous at the interface, $r/b = 1$. Different values for k_1b were chosen to show the behavior of the mode shapes in water and the PMMA. In the ET0 mode, as the frequency increases, the magnitudes of the axial components in the water increase as well. However, the magnitudes of these components are maximum at the interface, $r/b = 1$. In the PMMA, the magnitudes of the radial displacements become greater as frequency increases. Therefore, as k_1b increases, the magnitudes of the displacements at the interface and the magnitudes of the axial components in the PMMA side become larger. Recall that our source only directly excites the membrane in the range of $r/b < 0.85$. As a result, the ET0 mode cannot be excited by our source in the frequency range where large displacements at the interface and the PMMA are shown. The same reasoning applies to the excitation of the ET1 mode. At $k_1b = 2.7$, the magnitude of the axial displacement in the PMMA is nearly twice as large as that in water. Therefore our source cannot excite the ET1 mode at that frequency. However, at $k_1b = 3$, the magnitude

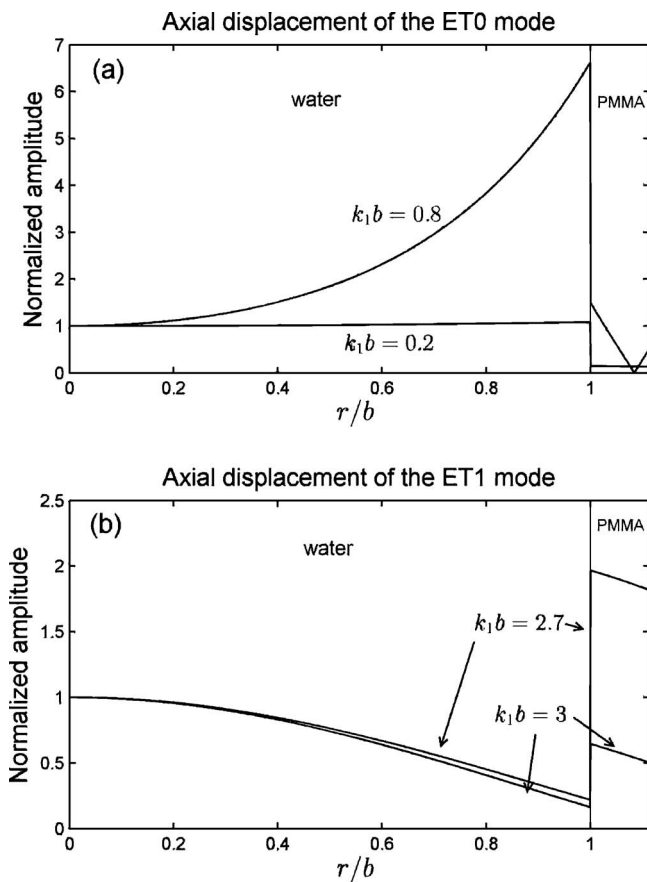


FIG. 10. Normalized axial displacements in water and in PMMA of the (a) ET0 and (b) ET1 modes as a function of the distance from the center of the tube at different values of (a) $k_1b=0.2$ and $k_1b=0.8$, and (b) $k_1b=2.7$ and $k_1b=3$. This figure, along with the attenuation characteristics of the modes shown in Fig. 9(b), explains the absence of observable ET0 and the ET1 modes over certain frequency ranges.

of the axial displacement in the PMMA side is less than that in the center of the tube, which means the ET1 mode may be excited at this frequency of $k_1b=3$. This corresponds to our observation that the ET1 mode starts to be measurable at frequencies in excess of $k_1b \approx 2.9$. As the frequency increases further to $k_1b=5$, the axial displacement in the PMMA become even smaller than it is for the $k_1b=3$ case, while the axial displacement in water is almost the same as for the $k_1b=3$ case (which is not shown here). Therefore, Fig. 10 explains why the ET0 mode is not observed in this experiment in the frequency range used and the ET1 mode is found in the region of $k_1b \geq 2.9$. Likewise, Fig. 11 explains why the ET2 and the ET3 modes are found at certain frequencies. Although it was not shown here, the axial displacement of the ET4 mode show significant phase change in the water side so that the piston-like acoustic source used here may not excite that mode.

Figure 9(b) shows the measurement of the normalized attenuation from the model that includes damping (solid curves) both in linear and the vertical logarithm scale. As explained in Sec. III, measurements by the PS method are denoted as filled symbols. Except for those, all other results are processed by the $k-\omega$ and the method described in Sec. III. The ET1, ET2, and ET3 modes are denoted as open circles, open triangles, and open squares, respectively. The

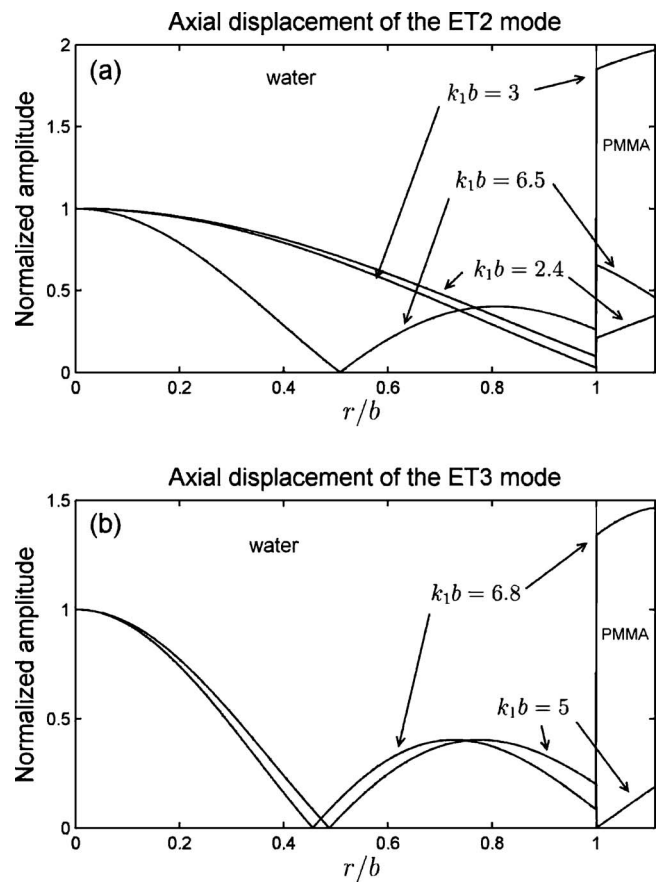


FIG. 11. Normalized axial displacements in water and in PMMA of the (a) ET2 and (b) ET3 modes as a function of the distance from the center of the tube at different values of (a) $k_1b=2.4$, $k_1b=3$, and $k_1b=6.5$, and (b) $k_1b=5$ and $k_1b=6.8$. This figure, along with the attenuation characteristics of the modes shown in Fig. 9(b), explains the absence of observable ET2 and the ET3 modes over certain frequency ranges.

order of the mode assigned to each data point has been found through the manual assignment of Fig. 9(a), where errors bars are smaller, as described earlier. While the error bars for attenuation are much greater than those in the phase velocity measurements of Fig. 9, the $k-\omega$ data (open symbols) show better agreement with theory than do the PS data [as in Fig. 9(a)], which has such large error bars as to make a meaningful comparison with theory difficult.

There are three possible candidate reasons for the discrepancies between the measured and predicted attenuations. The first is interference of the direct wave with energy reflected from the upper and lower ends of the water column. The measurement window was set at the minimum feasible, 2 ms, less than the 2.7 ms required for a 1500 m/s pulse to transit the tube twice, such that reflections from the base should not appear in the measurement window. However when the hydrophone is close to the top of the water column, such reflected pulses entered the time window for acquisition. However the overlapping nature of these is readily decoupled using the $k-\omega$ map. The second possible contribution to the discrepancy may be residual air bubbles. Although deliberate efforts made to remove such bubbles, very small bubbles could be stabilized in imperfectly wetted solids (e.g., at surface microcracks in the pipe wall, on hydrophones etc. as they move in and out of the water). The very small attenu-

ations predicted here would be far more sensitive to perturbation by such bubbles than would the phase speeds. The third possible contribution to the discrepancy is interference of the measured (and modeled) axisymmetric mode with non-axisymmetric modes. Though these are absent from the theory, they exist in the experiment. Energy invested in non-axisymmetric modes is clearly present in the data, for example as several bright features in Fig. 8(b) which occur outside the loci of the labeled axisymmetric modes. Interference at a particular measurement point in the waveguide involving modes not present in the theory could appear as attenuation in the more dominant mode, which is another argument for experimental schemes which move the measurement point along the length of the pipe as opposed to using fixed transducer positions.

Such discrepancies in attenuation will be very much smaller than the attenuation caused when dense populations of helium bubbles are deliberately injected into the mercury-filled steel pipes of the Spallation Neutron Source (SNS) at the Oak Ridge National Laboratory (ORNL), Tennessee. The authors hope to invert the changes in attenuation and sound speed to estimate the bubble population present. Bubbles in aqueous solution have been measured⁵⁴ to reduce high order modal sound speeds in cylinders of water to as low as 868 m/s. A persistent population of gas bubbles in mercury (built up adventitiously by the 60 Hz firing rate of the proton beam⁵⁵ or, if this is insufficient, through helium injection⁵⁶) is currently thought of as a potential mitigating⁵⁷⁻⁵⁹ measure against the cavitation erosion which occurs in the steel wall of the vessel containing the mercury. It is considered important to develop sensors which rely on the propagation and detection of acoustical waves in the mercury, for example to monitor the bubble population.^{50,60} Figures 12(a) and 12(b) show the predicted phase velocity and the attenuation of the propagating axisymmetric modes in the mercury-filled stainless steel pipe (of inner radius of 6.41 cm and wall thickness of 0.655 cm). The values used for the densities of the steel and the mercury are 7.9 and 13.5 g/cm³, respectively. Longitudinal and shear speeds of the sound in the stainless steel 304 (SS304) are 5.675 km/s and 3.141 km/s, respectively, and the corresponding Poisson's ratio is about 0.28. Shear and bulk viscosity coefficients for the mercury are 1.53 and 1.90 cP, respectively.⁶¹ The magnitudes of the viscosity coefficients for the mercury have similar order of magnitude to those for water. Hence, for simplicity, Eq. (6) with the elements in Appendix B can be used instead of the elements in Appendix A since the corresponding ϵ defined in Eq. (3) becomes large and the elements in Appendix A can be reduced to the elements in Appendix B. The complex solution to the mercury/steel pipe is obtained by the same method as was described in Sec. II C by substituting k_s , k_c , and k_1 with k'_s , k'_c , and k'_1 into the elements in Appendix B with the modification of the expression of k'_1 which includes the absorption caused by the thermal conduction. Mercury has a Prandtl number,²⁷ P_N , of 0.0266, and thermal absorption is greater than viscous absorption (in contrast to water, where $P_N=6.75$ and the effect of thermal conduction on the damping is at least 1000 times smaller than the viscous effect in

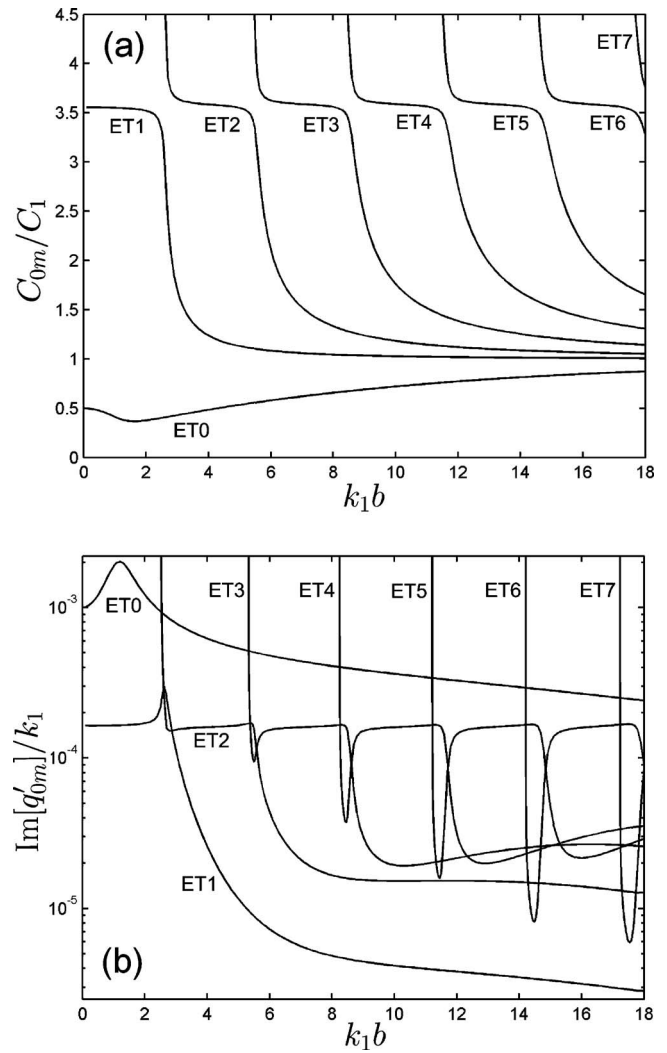


FIG. 12. Predicted normalized (a) phase velocities and (b) damping of the axisymmetric modes in the mercury-filled steel pipe as a function of normalized frequency. The material properties of the steel tube are described in Sec. IV. Throughout the frequency range, the attenuation of the ET0 mode is greater than that of the ET1 mode. The attenuation in the mercury/steel system is about one order of magnitude less than in the PMMA/water case.

water). In the mercury/steel pipe case, the complex wave-number, k'_1 , including the viscous and thermal effects, is expressed as follows:²⁷

$$k'_1 \approx k_1 + i \frac{\omega^2}{2\rho_L C_1^3} \left(\frac{4}{3} \eta + \eta_B + \frac{(\gamma-1)\kappa}{c_p} \right), \quad (13)$$

where γ is ratio of the heat capacities, c_p is specific heat at constant pressure, and κ is thermal conductivity. For mercury, the additional term inside the parenthesis, $(\gamma-1)\kappa/c_p$, is calculated as 7.62 cP which is about 4 times larger than the viscous coefficients of the mercury. The normalized shear absorption, γ_s , was obtained from measurements in the literature⁶² and the normalized longitudinal absorption, γ_c , was estimated from the theory,⁶³ giving values of $\gamma_c = 3.120 \times 10^{-4}$ and $\gamma_s = 7.638 \times 10^{-4}$. Note that these preliminary calculations assume perfect wetting of the steel by the mercury, which might not occur in practice.

Figure 12(a) shows the phase velocity of the modes normalized by the speed of sound in bulk mercury. Although the

numerical values are different, the general features and frequency dependence of the modes are very similar to the PMMA/water case shown in Fig. 3(a). The acoustical coupling between mercury and the steel is similar to that between water and the PMMA. The cut-off frequencies for this mercury/steel pipe are listed in Table II.

Figure 12(b) shows the predicted attenuation in the mercury contained in the steel pipe normalized by the real wave-number in the infinite body of the liquid mercury. As with the PMMA/water case shown in Fig. 5(a), the attenuation of the ET0 mode is larger than that of the higher modes above their cut-off frequencies, for the frequency range studied here. The attenuation in the mercury/steel system is about one order of magnitude less than in the PMMA/water case. Therefore, in the steel pipe filled with the bubble-free mercury, it is expected that the extra attenuation imparted by the presence of bubbles (which would be inverted to estimate the bubble size distribution) will be much larger, simplifying the problem.

V. CONCLUSIONS

Theoretical and experimental investigations have been carried out to predict the phase velocity and damping of the modes in a liquid-filled pipe, and hence to lay the foundation for estimating the dominant modes at a given frequency range in a PMMA tube which is filled with water. Several modes were experimentally found through the $k-\omega$ method, which gave clearer results than the PS method, and which can separate the modes in the wavenumber and frequency domain, and give an accurate result focusing on a particular mode. The dominant features in $k-\omega$ space match the theoretical ET1–ET3 modes in the limited frequency range of $2 < k_1 b < 7$. The measurements were compared with the theoretical calculations done by extending the Del Grosso's formulation into the complex domain. To obtain the complex solution, the damping of the tube material and liquid inside was incorporated into the formulation and the solution was found in complex space. The phase speed obtained from the real part of the solution matches with the lossless solution. However, when the viscosity of the liquid or the absorption by the elastic tube are not negligible, the phase speeds of the modes are expected to be changed as discussed in Sec. II C. The corresponding imaginary solution gives the damping of the mode. One subsonic mode, ET0, was not observed in our measurement since the source condition cannot excite the shape of the mode in this particular frequency range. The limited abilities of the source, when coupled to the tube in this way, to invest significant energies in the required frequencies and mode shapes explains the absence of other modes over certain frequency ranges, an effect which could be exacerbated by the larger attenuation that can occur at certain frequencies once a given mode has begun to propagate. Current simulation studies are ongoing to provide phase and group speeds, and attenuations, for comparison with the data and the theory presented in this paper. The theory was also applied to the case of mercury-filled steel pipes.

ACKNOWLEDGMENTS

This work is supported by the Oak Ridge National Laboratory (ORNL), Tennessee. ORNL is managed by UT-Battelle, LLC, under contract DE-AC05-00OR22725 for the U.S. Department of Energy. This work is also funded by the UK Science and Technology Research Council (Principle Investigator: T. G. Leighton). This formulation was developed to assist in understanding acoustic propagation in mercury-filled steel pipes at ORNL, in relation to neutron generation through Spallation Neutron Sources. The authors thank Bernie Riemer and Mark Wendel of ORNL for access to the facilities and helpful discussion of the problem and to Chris Densham, Ottone Caretta, and Tristan Davenne at the UK Science and Technology Research Council Rutherford Appleton Laboratory for advice and discussions. The authors are particularly grateful to Ron Roy of Boston University for helpful discussion on the problem.

APPENDIX A: ELEMENTS IN EQ. (6)

$$d_{11}^{(0)} = -\frac{J_1(\epsilon b)}{\epsilon J_0(\epsilon b)} \frac{E_m}{P_m} \left(1 - \frac{\mu_L E_m^L}{\mu_E E_m}\right),$$

$$d_{11}^{(1)} = \left(1 - \frac{\mu_L}{\mu_E}\right) \left(1 - \frac{J_1(\epsilon b)}{\epsilon b J_0(\epsilon b)}\right),$$

$$d_{13}^{(0)} = T_m \frac{J_1(\epsilon b)}{\epsilon J_0(\epsilon b)} \left(1 - \frac{\mu_L E_m^L}{\mu_E q_{0m}^2}\right),$$

$$d_{13}^{(1)} = \frac{E_m}{q_{0m}^2} - \frac{J_1(\epsilon b)}{\epsilon b J_0(\epsilon b)} - \frac{\mu_L}{\mu_E} \left(1 - \frac{J_1(\epsilon b)}{\epsilon b J_0(\epsilon b)}\right),$$

$$d_{21}^{(0)} = 0, \quad d_{21}^{(1)} = 1, \quad d_{23}^{(0)} = 0, \quad d_{23}^{(1)} = \frac{E_m}{q_{0m}^2},$$

$$d_{31}^{(0)} = \frac{1}{P_m} \left(E_m - \Delta \frac{\mu_L}{\mu_E} q_{0m}^2\right),$$

$$d_{31}^{(1)} = \frac{1}{b} \left[1 - \frac{\mu_L}{\mu_E} + \frac{b^2 J_0(X_{0m})}{X_{0m} J_1(X_{0m})} \left(\Delta q_{0m}^2 - \frac{\mu_L}{\mu_E} E_m^L\right)\right],$$

$$d_{33}^{(0)} = -T_m \left(1 - \Delta \frac{\mu_L}{\mu_E}\right),$$

$$d_{33}^{(1)} = \frac{1}{b} \left[1 - \frac{\mu_L}{\mu_E} + \frac{b^2 J_0(X_{0m})}{X_{0m} J_1(X_{0m})} \left(\Delta E_m - \frac{\mu_L}{\mu_E} E_m^L\right)\right],$$

$$d_{41}^{(0)} = \frac{E_m}{P_m}, \quad d_{41}^{(1)} = \frac{1}{d}, \quad d_{43}^{(0)} = -T_m, \quad d_{43}^{(1)} = \frac{1}{d},$$

where $\mu_E = \rho_E C_s^2$, $\mu_L = -i\omega\eta$, $E_m = q_{0m}^2 - k_s^2/2$, $E_m^L = q_{0m}^2 - i\rho_L\omega/(2\eta)$, and Δ is 0 in the inviscid case and 1 otherwise.

APPENDIX B: ELEMENTS IN EQ. (6) IN INVISCID LIMIT

$$d_{11}^{(0)} = d_{21}^{(0)} = 0, \quad d_{11}^{(1)} = d_{21}^{(1)} = 1,$$

$$d_{13}^{(0)} = d_{23}^{(0)} = 0, \quad d_{13}^{(1)} = d_{23}^{(1)} = \frac{E_m}{q_{0m}^2},$$

$$d_{31}^{(0)} = d_{41}^{(0)} = \frac{E_m}{P_m}, \quad d_{31}^{(1)} = d_{41}^{(1)} = \frac{1}{b}(1 + bQ_m),$$

$$d_{33}^{(0)} = d_{43}^{(0)} = -T_m, \quad d_{41}^{(1)} = d_{43}^{(1)} = \frac{1}{d},$$

where

$$Q_m = \frac{\rho_L \omega^2 b J_0(X_{0m})}{2\rho_E C_s^2 X_{0m} J_1(X_{0m})},$$

and when these elements are substituted into Eq. (6), the result is identical to the formulation by Lafleur and Shields.²

- ¹V. A. Del Grosso, "Analysis of multimode acoustic propagation in liquid cylinders with realistic boundary conditions—Application to sound speed and absorption measurements," *Acustica* **24**, 299–311 (1971).
- ²L. D. Lafleur and F. D. Shields, "Low-frequency propagation modes in a liquid-filled elastic tube waveguide," *J. Acoust. Soc. Am.* **97**, 1435–1445 (1995).
- ³H. Kwun, K. A. Bartels, and C. Dynes, "Dispersion of longitudinal waves propagating in liquid-filled cylindrical shells," *J. Acoust. Soc. Am.* **105**, 2601–2611 (1999).
- ⁴B. K. Sinha, T. J. Plona, S. Kostek, and S. Chang, "Axisymmetric wave propagation in fluid-loaded cylindrical shells. I: Theory," *J. Acoust. Soc. Am.* **92**, 1132–1155 (1992).
- ⁵V. N. R. Rao and J. K. Vandiver, "Acoustics of fluid-filled boreholes with pipe: Guided propagation and radiation," *J. Acoust. Soc. Am.* **105**, 3057–3066 (1999).
- ⁶R. Long, M. Lowe, and P. Cawley, "Attenuation characteristics of the fundamental modes that propagate in buried iron water pipes," *Ultrasonics* **41**, 509–519 (2003).
- ⁷J. E. Greenspon and E. G. Singer, "Propagation in fluids inside thick viscoelastic cylinders," *J. Acoust. Soc. Am.* **97**, 3502–3509 (1995).
- ⁸P. B. Nagy and A. H. Nayfeh, "Viscosity-induced attenuation of longitudinal guided waves in fluid-loaded rods," *J. Acoust. Soc. Am.* **100**, 1501–1508 (1996).
- ⁹L. Elvira-Segura, "Acoustic wave dispersion in a cylindrical elastic tube filled with a viscous liquid," *Ultrasonics* **37**, 537–547 (2000).
- ¹⁰C. R. Fuller and F. J. Fahy, "Characteristics of wave propagation and energy distributions in cylindrical elastic shells filled with fluid," *J. Sound Vib.* **81**, 501–518 (1982).
- ¹¹A. R. Briscoe and R. J. Pinnington, "Axisymmetric vibrational power measurement in empty and fluid filled pipes," *J. Sound Vib.* **192**, 771–791 (1996).
- ¹²J. M. Muggleton, M. J. Brennan, and R. J. Pinnington, "Wavenumber prediction of waves in buried pipes for water leak detection," *J. Sound Vib.* **249**, 939–954 (2002).
- ¹³C. Aristégui, M. J. S. Lowe, and P. Cawley, "Guided waves in fluid-filled pipes surrounded by different fluids," *Ultrasonics* **39**, 367–375 (2001).
- ¹⁴G. A. Maximov, E. V. Podjachev, and K. V. Horoshenkov, "Attenuation and scattering of axisymmetrical modes in a fluid-filled round pipe with internally rough walls," *J. Acoust. Soc. Am.* **123**, 1248–1259 (2008).
- ¹⁵T. G. Leighton, P. R. White, C. L. Morfey, J. W. L. Clarke, G. J. Heald, H. A. Dumbrell, and K. R. Holland, "The effect of reverberation on the damping of bubbles," *J. Acoust. Soc. Am.* **112**, 1366–1376 (2002).
- ¹⁶H. Medwin, "In situ acoustic measurements of microbubbles at sea," *J. Geophys. Res.* **82**, 971–976 (1977).
- ¹⁷K. W. Commander and R. J. McDonald, "Finite-element solution of the inverse problem in bubble swarm acoustics," *J. Acoust. Soc. Am.* **89**, 592–597 (1991).
- ¹⁸T. G. Leighton, S. D. Meers, and P. R. White, "Propagation through non-

- linear time-dependent bubble clouds and the estimation of bubble populations from measured acoustic characteristics," *Proc. R. Soc. London, Ser. A* **460**, 2521–2550 (2004).
- ¹⁹W. M. Tian, "Integrated method for the detection and location of underwater pipelines," *Appl. Acoust.* **69**, 387–398 (2008).
- ²⁰T. G. Leighton, D. G. Ramble, A. D. Phelps, C. L. Morfey, and P. P. Harris, "Acoustic detection of gas bubbles in a pipe," *Acust. Acta Acust.* **84**, 801–814 (1998).
- ²¹T. G. Leighton, A. D. Phelps, D. G. Ramble, and D. A. Sharpe, "Comparison of the abilities of eight acoustic techniques to detect and size a single bubble," *Ultrasonics* **34**, 661–667 (1996).
- ²²T. G. Leighton, D. G. Ramble, and A. D. Phelps, "The detection of tethered and rising bubbles using multiple acoustic techniques," *J. Acoust. Soc. Am.* **101**, 2626–2635 (1997).
- ²³P. S. Wilson, R. A. Roy, and W. M. Carey, "An improved water-filled impedance tube," *J. Acoust. Soc. Am.* **113**, 3245–3252 (2003).
- ²⁴W. J. Jacobi, "Propagation of sound waves along liquid cylinders," *J. Acoust. Soc. Am.* **21**, 120–127 (1949).
- ²⁵T. C. Lin and G. W. Morgan, "Wave propagation through fluid contained in a cylindrical, elastic shell," *J. Acoust. Soc. Am.* **28**, 1165–1176 (1956).
- ²⁶K. Baik, J. Jiang, and T. G. Leighton, "Theoretical investigation of acoustic wave propagation in a liquid-filled cylinder," ISVR Technical Report No. TR 329, The Institute of Sound and Vibration Research, University of Southampton, Southampton, UK, 2009.
- ²⁷L. E. Kinsler, A. R. Frey, A. B. Coppens, and J. V. Sanders, *Fundamentals of Acoustics*, 4th ed. (Wiley, New York, 2000), Chap. 8, pp. 210–218.
- ²⁸National Physical Laboratory, "Kaye & Laby: Tables of physical & chemical constants," http://www.kayelaby.npl.co.uk/general_physics/2_2/2_2_3.html (Last viewed 1/28/2010).
- ²⁹B. T. Hefner and P. L. Marston, "Backscattering enhancements associated with sub-sonic Rayleigh waves on polymer spheres in water: Observation and modeling for acrylic spheres," *J. Acoust. Soc. Am.* **107**, 1930–1936 (2000).
- ³⁰B. Hartmann and J. Jarzynski, "Ultrasonic hysteresis absorption in polymers," *J. Appl. Phys.* **43**, 4304–4312 (1972).
- ³¹T. N. Grigsby and E. J. Tajchman, "Properties of Lamb waves relevant to the ultrasonic inspection of thin plates," *IRE Trans. Ultra. Eng.* **8**(1), 26–33 (1961).
- ³²J. M. Muggleton, M. J. Brennan, and P. W. Linford, "Axisymmetric wave propagation in fluid-filled pipes: Wavenumber measurements in in vacuo and buried pipes," *J. Sound Vib.* **270**, 171–190 (2004).
- ³³T. G. Leighton, W. L. Ho, and R. Flaxman, "Sonoluminescence from the unstable collapse of a conical bubble," *Ultrasonics* **35**, 399–405 (1997).
- ³⁴T. G. Leighton, A. D. Phelps, B. T. Cox, and W. L. Ho, "Theory and preliminary measurements of the Rayleigh-like collapse of a conical bubble," *Acust. Acta Acust.* **84**, 1014–1024 (1998).
- ³⁵Y. Yin and K. V. Horoshenkov, "The attenuation of the higher-order cross-section modes in a duct with a thin porous layer," *J. Acoust. Soc. Am.* **117**, 528–535 (2005).
- ³⁶T. G. Leighton and R. C. P. Evans, "The detection by sonar of difficult targets (including centimetre-scale plastic objects and optical fibres) buried in saturated sediment," *Appl. Acoust.* **69**, 438–463 (2008).
- ³⁷T. G. Leighton, "The detection of buried marine targets," *Appl. Acoust.* **69**, 385–386 (2008).
- ³⁸A. D. Pierce, *Acoustics: An Introduction to Its Physical Principles and Applications* (American Institute of Physics, Melville, NY, 1994), Chap. 10, pp. 531–534.
- ³⁹T. A. Litovitz and C. M. Davis, in *Physical Acoustics: Principles and Methods*, edited by W. P. Mason (Academic, New York, 1964), Vol. **2**, Chap. 5, pp. 281–349.
- ⁴⁰H. Wright, C. S. N. Faraday, E. F. T. White, and L. R. G. Treloar, "The elastic constants of oriented glassy polymers," *J. Phys. D: Appl. Phys.* **4**, 2002–2014 (1971).
- ⁴¹W. P. Mason and H. J. McSkimin, "Attenuation and scattering of high frequency sound waves in metals and glasses," *J. Acoust. Soc. Am.* **19**, 464–473 (1947).
- ⁴²W. Roth, "Scattering of ultrasonic radiation in polycrystalline metals," *J. Appl. Phys.* **19**, 901–910 (1948).
- ⁴³C. Zucker, "Ultrasonic absorption in metals at elevated temperatures," *J. Acoust. Soc. Am.* **28**, 721–723 (1956).
- ⁴⁴D. H. Johnson and D. E. Dudgeon, *Array Signal Processing: Concepts and Techniques* (Prentice-Hall, Englewood Cliffs, NJ, 1993), Chap. 2, pp. 21–30.
- ⁴⁵W. Sachse and Y. H. Pao, "On the determination of phase and group

- velocities of dispersive waves in solids," *J. Appl. Phys.* **49**, 4320–4327 (1978).
- ⁴⁶F. Peters and L. Petit, "A broad band spectroscopy method for ultrasound wave velocity and attenuation measurement in dispersive media," *Ultrasonics* **41**, 357–363 (2003).
- ⁴⁷M. R. Osborne and G. K. Smyth, "A modified Prony algorithm for exponential function fitting," *SIAM J. Sci. Comput. (USA)* **16**, 119–138 (1995).
- ⁴⁸J. Vollmann, R. Brey, and J. Dual, "High-resolution analysis of the complex wave spectrum in a cylindrical shell containing a viscoelastic medium: Part II. Experimental results versus theory," *J. Acoust. Soc. Am.* **102**, 909–920 (1997).
- ⁴⁹P. Dupuis, T. Sels, J. Driesen, and R. Belmans, "Exponential parameters measurement using a modified Prony method," in *IMTC 2004-IEEE Instrumentation and Measurement, Technology Conference, Como, Italy* (2004), pp. 1590–1594.
- ⁵⁰G. T. Yim and T. G. Leighton, "Real-time on-line monitoring of ceramic 'slip' in pottery pipe-lines using ultrasound," *Ultrasonics* **50**, 60–67 (2010).
- ⁵¹A. Cummings, "Stiffness control of low frequency acoustic transmission through the walls of rectangular ducts," *J. Sound Vib.* **74**, 351–380 (1981).
- ⁵²R. J. Astley, A. Cummings, and N. Sormaz, "A finite element scheme for acoustic propagation in flexible-walled ducts with bulk-reacting liners, and comparison with experiment," *J. Sound Vib.* **150**, 119–138 (1991).
- ⁵³Neptune Sonar LTD, Manual of 4008 SN 18852 cylindrical transducer, East Yorkshire (2006), pp. 1–12.
- ⁵⁴P. R. Birkin, T. G. Leighton, J. F. Power, M. D. Simpson, A. M. L. Vincotte, and P. F. Joseph, "Experimental and theoretical characterisation of sonochemical cells. Part I: Cylindrical reactors and their use to calculate speed of sound," *J. Phys. Chem. A* **107**, 306–320 (2003).
- ⁵⁵N. J. Manzi, P. V. Chitnis, R. G. Holt, R. A. Roy, R. O. Cleveland, B. Riemer, and M. Wendel, "Detecting cavitation in mercury exposed to a high-energy pulsed proton beam," *J. Acoust. Soc. Am.* **127**, 2231–2239 (2010).
- ⁵⁶H. Kogawa, T. Shobu, M. Futakawa, A. Bucheeri, K. Haga, and T. Naoe, "Effect of wettability on bubble formation at gas nozzle under stagnant condition," *J. Nucl. Mater.* **377**, 189–194 (2008).
- ⁵⁷T. Lu, R. Samulyak, and J. Glimm, "Direct numerical simulation of bubbly flows and application to cavitation mitigation," *J. Fluids Eng.* **129**, 595–604 (2007).
- ⁵⁸B. W. Riemer, P. R. Bingham, F. G. Mariam, and F. E. Merrill, "Measurement of gas bubbles in mercury using proton radiography," in *Proceedings of the 8th International Topical Meeting on Nuclear Applications and Utilization of Accelerators ACCAPP '07* (2007), pp. 531–537.
- ⁵⁹K. Okita, S. Takagi, and Y. Matsumoto, "Propagation of pressure waves, caused by thermal shock, in liquid metals containing gas bubbles," *J. Fluid Sci. Technol.* **3**, 116–128 (2008).
- ⁶⁰M. A. Ainslie and T. G. Leighton, "Near resonant bubble acoustic cross-section corrections, including examples from oceanography, volcanology, and biomedical ultrasound," *J. Acoust. Soc. Am.* **126**, 2163–2175 (2009).
- ⁶¹J. Jarzynski, "Ultrasonic propagation in liquid Bismuth and Mercury," *Proc. Phys. Soc. London* **81**, 745–750 (1963).
- ⁶²T. Hirone and K. Kamigaki, "Attenuation of the ultrasonic waves in metals. II: Stainless steel," Report No. 912, Research Institute for Iron, Steel and Other Metals, Tohoku University, Sendai, Japan, 1958.
- ⁶³E. P. Papadakis, "Rayleigh and stochastic scattering of ultrasonic waves in steel," *J. Appl. Phys.* **34**, 265–269 (1963).